Journal of Computational Physics 397 (2019) 108874

Contents lists available at ScienceDirect

Journal of Computational Physics

www.elsevier.com/locate/jcp

Bayesian estimation of physical and geometrical parameters for nanocapacitor array biosensors

Benjamin Stadlbauer [a,*], Andrea Cossettini [b], José A. Morales E. [a], Daniel Pasterk [a], Paolo Scarbolo [b], Leila Taghizadeh [a], Clemens Heitzinger [a], Luca Selmi [c]

[a] Vienna University of Technology, Wiedner Hauptstrasse 8–10, 1040 Vienna, Austria
[b] University of Udine, via delle Scienze 206, 33100 Udine, Italy
[c] University of Modena and Reggio Emilia, Via P. Vivarelli 10, 41125 Modena, Italy

ARTICLE INFO

Article history:
Received 20 December 2018
Received in revised form 11 July 2019
Accepted 31 July 2019
Available online 6 August 2019

Keywords:
Bayesian estimation
MCMC
Nanoelectrode arrays
Nanosensors
Uncertainty quantification

ABSTRACT

Massively parallel nanosensor arrays fabricated with low-cost CMOS technology represent powerful platforms for biosensing in the Internet-of-Things (IoT) and Internet-of-Health (IoH) era. They can efficiently acquire "big data" sets of dependable calibrated measurements, representing a solid basis for statistical analysis and parameter estimation.
In this paper we propose Bayesian estimation methods to extract physical parameters and interpret the statistical variability in the measured outputs of a dense nanocapacitor array biosensor. Firstly, the physical and mathematical models are presented. Then, a simple 1D-symmetry structure is used as a validation test case where the estimated parameters are also known *a-priori*. Finally, we apply the methodology to the simultaneous extraction of multiple physical and geometrical parameters from measurements on a CMOS pixelated nanocapacitor biosensor platform.

1. Introduction

One of the tasks in uncertainty quantification (UQ) is to identify which variables are uncertain in a system under study and their effect on the observables. UQ is becoming increasingly important in nanoelectronics and all its applications due to the many non-negligible sources of fluctuations and variability which affect nanoscale devices [1,2] and in turn constrain the design of functional electronics. UQ is even more important for nanoelectronic biosensors, where biological noise adds to traditional electrical noise sources and contributes to determine the limit of detection (LoD).

A popular UQ method is Bayesian estimation (BE) [3–5], where prior knowledge is updated after new information of the system is obtained, for instance by means of measurements, and included in the posterior knowledge by means of Bayes' theorem from probability theory [6]. BE provides not only a single value, but also an estimate of its expected statistical distribution. Parameter extraction by means of classical inverse-modeling techniques [7,8], instead, suffers serious limitations,

* Corresponding author.
E-mail addresses: benjamin.stadlbauer@asc.tuwien.ac.at (B. Stadlbauer), cossettini.andrea@spes.uniud.it (A. Cossettini), jose.morales@asc.tuwien.ac.at (J.A. Morales E.), daniel.pasterk@tuwien.ac.at (D. Pasterk), scarbolo.paolo@spes.uniud.it (P. Scarbolo), leila.taghizadeh@tuwien.ac.at (L. Taghizadeh), clemens.heitzinger@tuwien.ac.at (C. Heitzinger), luca.selmi@unimore.it (L. Selmi).

https://doi.org/10.1016/j.jcp.2019.108874
0021-9991/

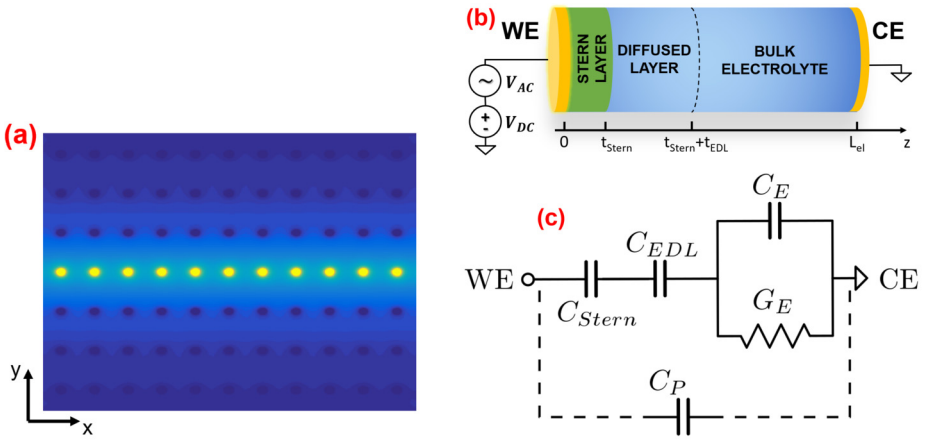

Fig. 1. (a): AC potential distribution over an 11×7 electrodes portion of the array simulated with the model of Sect. 2.2. Electrolyte with $n_0^\infty = 150$ mM NaCl in water. $f = 50$ MHz [26,27]. The central row is activated by a $V_{DC} + V_{AC}$ potential, therefore acting as a set of working electrodes; all other rows are grounded counterelectrodes. (b): Sketch of a simple 1D-symmetry structure capturing the essential physics of the nanoelectrode. Working electrode (WE), Stern layer, diffused layer, electrolyte and counter electrode (CE). (c): Lumped elements equivalent circuit to represent the admittance Y of the 1D system in (b) according to Gouy-Chapman-Stern theory. The equivalent circuit can also model the admittance of an individual nanoelectrode in the real biosensor array provided the parasitic capacitance C_P is added.

because the solution comes without any estimate of its uncertainty. Furthermore, ill-posed nonlinear inverse problems may not have unique solutions, requiring a separate verification of the correctness of the result.

In the following, we discuss in detail the use of Bayesian estimation techniques to interpret the statistical variability in the measured outputs of a nanocapacitor array biosensor for impedance spectroscopy applications [5,9,10], relevant to upward scaling (more electrodes, more chips) as well as downward scaling (smaller radii of the electrodes and smaller pitch). The platform provides an ideal case-study for a larger category of scalable, massively parallel arrays amenable to fabrication with state-of-the-art CMOS nanoelectronic technologies [11–19], and thus of great potential relevance for future biosensing applications in the trillion sensor vision of the Internet of Things [20]. The massively-parallel implementation enables to collect in a very efficient way large amounts of data concerning individual nanoscale objects in controlled conditions, thus providing the large datasets required by BE algorithms.

Although BE techniques have been used for UQ in several applications [21–24], to the best of our knowledge this work constitutes the first BE study of massively parallel nanocapacitor array biosensors. The results illustrate the ability of the proposed UQ method to support the extraction of relevant geometrical and physical system parameters and to provide insight on the sources of variability.

To set the stage and notation, we describe the physical system and its model in Sect. 2 and the extraction technique in Sect. 3. Sections 4–5 illustrate the application of the technique to actual measurements.

2. Physical and mathematical modeling of nanoelectrode array biosensors

2.1. The biosensor platform

We refer to the versatile biosensor platform of [11–14] as a realistic reference test case. The platform consists of 256×256 gold nanoelectrodes with $r_{\text{el}} = 90$ nm nominal radius and $p_x \times p_y = 600$ nm $\times$ 720 nm inter-electrodes pitch along the x (row) and y (column) directions, respectively. The array is scanned by exciting one row at a time (see Fig. 1a). Following a charge-based capacitance measurement principle, CBCM [11,25], the capacitance of each nanoelectrode is measured by alternatively charging and discharging them at frequency $f \in [1; 70]$ MHz, resulting in an approximately square-wave-like voltage waveform at the node of the nanoelectrode. By integrating the charging current, the average charge per cycle transferred to the nanoelectrode is obtained and converted to digital format, as explained in detail in [11]. In the following, we denote the experimentally measured nanoelectrode capacitance by C_{exp}.

A number of geometrical and physical parameters have an influence on C_{exp}, each with its own random variability. For instance, the radius r_{el}, protrusion and roughness of the electrodes, the concentration of ions in the electrolyte, the polarization of water molecules near to the nanoelectrode surface (which affects the dielectric permittivity ε). In the following we will exemplify the analysis of a few of these.

The basic Physics is well captured by the simple 1D-symmetry structure depicted in Fig. 1(b). An electrolyte region is defined between one ideally polarizable working electrode, WE (i.e. one electrode that carries no DC current), biased at DC voltage $V_{DC} = 0\,V$ and the grounded counter electrode (CE). A small-signal AC excitation, V_{AC} is added to the WE DC potential. According to established electrolyte physics [28], ions and water molecules create a thin layer of dipoles at the interface between the WE and the electrolyte (Stern layer) with reduced dielectric permittivity ($\varepsilon_{\text{Stern}}$) with respect to

the bulk electrolyte. The Stern layer extends into a thicker diffusion layer with non-negligible space charge density with respect to the neutral bulk electrolyte. Together, they form the so-called Gouy-Chapman-Stern electrical double layer (EDL) [29–32]. The EDL plays a fundamental role in screening analytes, reducing the sensitivity; it is thus important to investigate accurately its properties.

The response of an individual nanoelectrode in the array of the biosensor platform, thoroughly explored in Section 5, can be modeled with the equivalent circuit of Fig. 1(c), where symbols in solid lines represent the individual working electrode and the extra capacitance C_P represents the parasitic coupling to adjacent counter electrodes [11]. Both the simple 1D system (Fig. 1(b)) and the nanoelectrode array (Fig. 1(a)) configurations will be studied in the following.

2.2. The PB-PDD modeling framework

For the sake of a self-contained paper, we report below the essentials of a numerical modeling framework adequate to describe the nanocapacitor array and analogous biosensor systems [11–14,33–40]. It is given by the Poisson-Boltzmann (PB) equation in the equilibrium DC regime, and the Poisson-drift-diffusion equations (PDD) for the small-signal, linearized AC regime [41–50].

2.2.1. DC formulation

Under the equilibrium conditions that describe the system in Fig. 1 at $V_{DC} = 0$ V, the model equation for the DC problem is the so-called Poisson-Boltzmann (PB) equation [28]

$$\nabla \cdot (\varepsilon(\vec{r})\nabla V_0(\vec{r})) + \rho_{0_f}(\vec{r}) + q\sum_{m=1}^{N_{ions}} Z_m n_{0,m}^{\infty} \exp\left(-\frac{Z_m q\left(V_0(\vec{r}) - V_{ref}\right)}{k_B T}\right) = 0, \tag{1}$$

where $V_0(\vec{r}) \in \mathcal{V}$ is the DC potential, q is the elementary charge, k_B is the Boltzmann constant, ε is the dielectric permittivity, and T is the absolute temperature. For the simple 1D system, the spatial coordinate $\vec{r}$ is the z-coordinate $z \in [0, L_{\text{el}}]$. The charge density is given by spatially immobilized charges ($\rho_{0,f}$) and mobile ion charges in the electrolyte ($\rho_{0,m}$); this is the summation term in Eq. (1), which depends on the signed valence Z_m and the bulk concentration $n_{0,m}^{\infty}$ of the m-th ionic species, the number of ions species (N_{ions}), and the reference potential V_{ref} in the bulk of the electrolyte. Dirichlet boundary conditions are used on the electrodes, Neumann ones elsewhere.

2.2.2. AC formulation

The AC model is formulated in the time-harmonic small-signal (i.e. linearized) approximation. Under this assumption, we obtain the AC Poisson equation

$$\nabla \cdot \left(\varepsilon(\vec{r})\nabla \tilde{V}(\vec{r})\right) + \sum_{m=1}^{N_{ions}} \frac{q^2 Z_m^2}{k_B T} n_{0_m}(\vec{r}) \left(\tilde{\phi}_m(\vec{r}) - \tilde{V}(\vec{r})\right) = 0, \tag{2}$$

where $\tilde{V}(\vec{r})$ is the electrostatic potential phasor, $\tilde{\phi}_m(\vec{r})$ is the pseudo-potential of the m-th ionic species, $n_{0_m}(\vec{r})$ is the DC ion concentration of the m-th ionic species and $\tilde{n}_m(\vec{r}) = n_{0_m}(\vec{r})\ qZ_m\ \left(\tilde{\phi}_m(\vec{r}) - \tilde{V}(\vec{r})\right)/(k_B T))$ is the corresponding AC phasor [47].

The currents are described by the drift-diffusion equations

$$qZ_m\mu_m \nabla \cdot \left(n_{0_m}(\vec{r})\nabla\tilde{\phi}_m(\vec{r})\right) - j\omega n_{0_m}(\vec{r})\frac{qZ_m}{k_B T}\left(\tilde{\phi}_m(\vec{r}) - \tilde{V}(\vec{r})\right) = 0 \tag{3}$$

after linearization (again, assuming that the electrolyte is in equilibrium and no DC current is flowing), where μ_m is the mobility of the m-th ionic species, j is the imaginary unit, and ω is the angular frequency. This allows to compute the AC current density $\tilde{J}$ as the summation of the displacement $\tilde{J}_D$ and ionic current densities $\tilde{J}_m$ as

$$\tilde{J} = \tilde{J}_D + \sum_m \tilde{J}_m = -j\omega\varepsilon\nabla\tilde{V}(\vec{r}) - \sum_m q^2 Z_m^2 \mu_m n_{0_m} \nabla\tilde{\phi}_m(\vec{r}). \tag{4}$$

This completes the PDD formulation. The working (WE) and counter (CE) electrodes are modeled by Dirichlet boundary conditions, whereas a Neumann condition is imposed to the other boundaries. More details on the calculation of the electrode currents can be found in [47]. The electrode admittance is given by $\tilde{Y} = \tilde{I}/V_{AC}$, where V_{AC} is the WE's AC potential and $\tilde{I}$ is the total AC current at the electrode ($\tilde{I} = \text{Area} \times \tilde{J}$ for the 1D structure in Fig. 1).

2.3. Analytical and numerical simulations

Numerical simulations of the biosensor systems in Fig. 1 reported below have been carried out with ENBIOS, a custom control-volume finite-element method (CVFEM) full-3D numerical simulator which solves the PB and PDD equations (1)–(3)

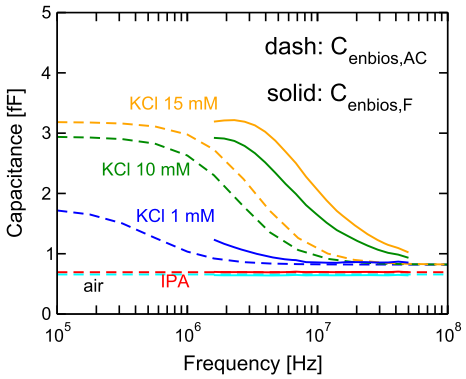

Fig. 2. Simulated $C_{enbios,AC}$ and $C_{enbios,F}$ capacitance spectra (including a $C_P = 0.65$ fF) for one nanoelectrode of the array in Fig. 1 (a) for different ambient. The responses in dry and IPA (IsoPropyl Alcohol) exhibit a flat frequency spectrum due to the very large R_E. Curves in electrolyte show the typical response in the presence of ions, i.e. two distinct capacitance values in the low- and high- frequency limit. The $C_{enbios,F}$ spectra account for the actual shape of the nanoelectrode voltage waveforms) and are limited to the frequency range of operation of the experimental biosensor platform.

self-consistently and computes the terminal currents $\tilde{I}$ and the admittances $\tilde{Y}$ [47,51,52]. Tetrahedral grids are created via the netgen mesh generator [53]. Unless otherwise stated, the Stern layer is modeled as a dielectric with thickness $t_{\text{Stern}} = 2.5$ Å and permittivity $\varepsilon_{\text{Stern}} = \varepsilon_{r,\text{Stern}}\varepsilon_0 = 7\varepsilon_0$ [54] (where ε_0 is the vacuum permittivity and $\varepsilon_{r,\text{Stern}}$ represents the relative Stern permittivity) consistently with the standard values of capacitance per unit area of the compact layer in [55]. As for the array of Fig. 1(a), the admittance at the central electrode of a 7×7 array is considered; this array size is sufficient to mitigate the effects of the domain boundaries.

Analytical calculations for the simple 1D system of Fig. 1(b) can be worked out in the PB-PDD formalism for the simple case where the DC potential of the WE is zero. The solution can be interpreted with the equivalent circuit drawn with solid lines in Fig. 1(c) (neglecting C_P), where the Stern layer capacitance C_{Stern}, the EDL capacitance C_{EDL}, and the bulk electrolyte conductance and capacitance G_E and C_E are given by [54]

$$c_{\text{Stern}} = \frac{C_{\text{Stern}}}{A} = \frac{\varepsilon_{\text{Stern}}}{t_{\text{Stern}}}, \qquad c_{\text{EDL}} = \frac{C_{\text{EDL}}}{A} = \frac{\varepsilon_{\text{el}}}{\lambda_D}, \qquad c_E = \frac{C_E}{A} = \frac{\varepsilon_{\text{el}}}{L_{\text{el}}}, \qquad g_E = \frac{G_E}{A} = \xi c_E, \tag{5}$$

where A is the cross-section area of the 1D-symmetry structure, t_{Stern} is the thickness of the Stern layer, $\varepsilon_{\text{el}} \simeq 78\varepsilon_0$ is the permittivity of the bulk electrolyte, L_{el} is the length of the electrolyte region, $\xi = \sigma_{\text{el}}/\varepsilon_{\text{el}} = 2q^2\mu n_0/\varepsilon_{\text{el}}$ is the electrolyte dielectric cut-off angular frequency and $\lambda_D = \sqrt{k_B T \varepsilon_{\text{el}}/2q^2 n_0}$ is the Debye length (which sets the thickness of the EDL, σ_{el} is the electrolyte conductivity, and μ and n_0 are the mobility and concentration of the ions, under the assumption of having a 1:1 symmetric electrolyte [54]).

The analytical expression of the capacitive component of the small signal admittance for the circuit model in Fig. 1(b) is given by

$$C_{\text{a.m.}}(\omega) = \frac{\Im[Y(\omega)]}{\omega} = \frac{1}{\omega}\Im\left[\left(\frac{1}{j\omega C_{\text{Stern}}} + \frac{1}{j\omega C_{\text{EDL}}} + \frac{1}{G_E + j\omega C_E}\right)^{-1}\right]. \tag{6}$$

In Sect. 4, we will make use of this analytical model ("a.m.") of the simple 1D-structure of Fig. 1(b) to validate the BE methodology. To this end, we will also perform ENBIOS numerical simulations of the same system to determine $C_{\text{enbios,AC}} = \Im\left[\tilde{Y}(\omega)/\omega\right]$, where $\tilde{Y}(\omega)$ is the admittance at the WE terminal. Finally, in Sect. 5, we will apply the BE methodology to the real nanobiosensor platform and we will compare simulation results to measurements. In this case, the experimental capacitance C_{exp} is obtained from a square wave-like switching setup (CBCM method). Hence, C_{exp} is not directly comparable to the time-harmonic small signal capacitance $C_{\text{enbios,AC}}$ computed with ENBIOS.

To address this matter, a *switching capacitance* was introduced in [11] (C_{SW}), which accounts for the charging/discharging process and the rich harmonic content of the square wave signals. Here, we further improve the accuracy of this calculation by introducing corrections to the switching model, resulting in a new formulation of the switching capacitance, denoted $C_{\text{enbios,F}}$, that also accounts for non-idealities and glitches of the nanoelectrode voltage waveforms. $C_{\text{enbios,F}}$ can be obtained from ENBIOS AC small signal simulations (essentially by means of Fourier series expansion of the AC small signal terminal current $\tilde{I}$, which enables to obtain the response to an arbitrarily-shaped input voltage waveform [56,57]), but the detailed description of its derivation goes beyond the scope of this work. Thus, when making use of experimental data C_{exp} in Sect. 5, we will rely on $C_{\text{enbios,F}}$ calculations for the analyses. Fig. 2 shows typical $C_{\text{enbios,AC}}$ and $C_{\text{enbios,F}}$ spectra. The difference reflects the multi-tone content of the electrode voltage and current spectra. Consistently with the circuit model of Fig. 1(c), two distinct capacitance levels are visible in the low- and high- frequency limit when we consider electrolytes. Both low- and high-frequency operation will be inspected in the following.

3. Bayesian inversion

3.1. Statistical model and Bayes' theorem

To set the stage for the description of the method we start by recalling that errors η due to measurement and modeling can be represented by means of random variables. For a given random variable M representing the information provided by measurements, for which we have a physical model $g(Q)$ dependent on a random variable Q (with realizations $q = Q(w)$) representing parameters, the statistical model

$$M - g(Q) = \eta, \tag{7}$$

holds. Here, w is an element of a probability space Ω_w. For vector quantities M and η, which represent different measurements M_i, we assume that the errors η_i are additive, independent and identically distributed (IID), unbiased and mutually independent from Q. Note that q can be a vector of realizations of parameters q_i as well, with an associated probability density function (PDF) providing information about them.

Assuming the probability measures above have PDFs, Bayes' theorem can be formulated specifically for the purposes of inverse modeling or parameter estimation. We denote the prior probability density function for the realizations q of the random parameters Q by $\pi_0(q)$, and a realization of the measurement M by m. Then the posterior density of Q, given the measurement m, can be expressed as

$$\pi(q|m) = \frac{\pi(m|q)}{\pi(m)}\pi_0(q) = \frac{\pi(m|q)\pi_0(q)}{\int_{\Omega_q}\pi(m|q)\pi_0(q)dq}, \tag{8}$$

where Ω_q is the space of parameters q.

A prior PDF π_0 reflects our knowledge of the parameters prior to observations. Our objective is to obtain a posterior PDF that incorporates the new knowledge of the acquired observations. This posterior is the solution of the inverse problem of parameter estimation via Bayesian techniques. In [58], Bayesian inversion for the nonlinear Poisson-Boltzmann equation in the measure-theoretic framework has been discussed, and well-definedness and well-posedness of the resulting posterior measures obtained from the Bayesian technique have been proved. In other words, the Bayesian approach to inverse problems is then to find the posterior probability density function $\pi(q|m)$ given the measurements M.

3.2. Markov chain Monte Carlo and the Metropolis-Hastings algorithm

At first sight it would seem that—in order to use Eq. (8)—we would have to compute the possibly high-dimensional integral $\int_{\Omega_q}\pi(m|q)\pi_0(q)dq$, which is costly. For a high-dimensional parameter space it would force us to resort to integration techniques such as Monte Carlo methods. Fortunately, numerical methods such as Markov Chain Monte Carlo (MCMC) render the computation of this high-dimensional integral superfluous.

Moreover, more sophisticated MCMC techniques have been developed [59], such as ensemble MCMC [60], multiple-try MCMC [61], and Hamiltonian MCMC [62–64] algorithms, where the latter, for example, tries to explore more regions of the parameter space via the introduction of an artificial "momentum" variable and then using Hamiltonian dynamics.

In this work, we use an MCMC method known as the random-walk Metropolis-Hastings (MH) algorithm. It is summarized here. The choices made to apply it to the problems under study are described in the next section.

The proposal distribution J must be chosen to ensure that the Markov chain is irreducible and aperiodic, because then it can be shown that a unique stationary distribution exists. It is also known that if the transition probabilities of a Markov chain satisfy the detailed-balance condition, then it converges to the stationary distribution. Therefore, after having chosen a proposal distribution, the acceptance ratio α is defined such that the Markov chain satisfies the detailed-balance condition for transition probabilities given by the sought posterior distribution. Consequently, the Markov chain constructed by the Metropolis-Hastings algorithm converges to the posterior distribution. The posterior distribution can still be seen as the products $\pi(m|q^*)\pi_0(q^*)$ and $\pi(m|q_{k-1})\pi_0(q_{k-1})$ in the acceptance ratio.

It is an important feature of this algorithm that it uses only the ratios of the likelihood π and the prior distribution π_0 occur in the calculations so that the (computationally expensive) integral in the denominator of (8) is never calculated.

The beginning of the Markov chain, i.e., the *burn-in period*, must be discarded. In practice, it is often not obvious how long the burn-in period should be. However, there are tests to instill confidence in the convergence of a Markov chain, and more on this subject can be found, for example, in [65,66].

The posterior distribution is absolutely continuous with respect to the prior, so a good choice of the latter is important. Therefore, if the initial guess is bad, convergence to the true value may be very slow. In this case, iterating the extraction procedure allows to reach the correct solution subsequently. Iterations are performed by running a first extraction, fitting the resulting posterior distribution, and repeating the extraction using this fitted distribution as a new prior. The number of iterations needed to reach a given precision varies depending on the choice of the first prior. This will be discussed in Sect. 4.1.3.

All algorithms for Bayesian inversion in this work have been implemented in the Julia programming language [67].

Algorithm 1: Metropolis-Hastings.

Data: Prior distribution $\pi_0(q)$;
the likelihood $\pi(m|q)$ of a measurement m given a parameter value q;
initial parameter value q_0 such that $\pi_0(q_0) > 0$;
proposal distribution $J(q \to q')$;
the number N_{samples} of samples to be generated.
Result: Posterior distribution $\pi(q)$ of the parameter values (and hence its mean, confidence intervals, etc.).

Initialization;
for $k = 1 : N_{\text{samples}}$ **do**
propose the next sample q^* according to the proposal distribution $J(q_{k-1} \to q^*)$;
compute the acceptance ratio

$$\alpha := \min\left(1, \frac{\pi(m|q^*)\pi_0(q^*)J(q* \to q_{k-1})}{\pi(m|q_{k-1})\pi_0(q_{k-1})J(q_{k-1} \to q^*)}\right), \tag{9}$$

where simplifications can be made depending on the special forms for π, π_0, and J;
cast a uniformly distributed random value $\chi \sim U(0,1)$;
define the next value q_k of the Markov chain as

$$q_k := \begin{cases} q^* & \chi \le \alpha, \\ q_{k-1} & \chi > \alpha. \end{cases}$$

end

Postprocessing: remove the *burn-in period*; calculate any statistics of interest such as the sample mean of the Markov chain. (The posterior $\pi(q)$ can be represented by means of a kernel density estimator (KDE) or the next iteration of the algorithm.)

4. Numerical results for stern layers and electrolyte concentrations

Here the procedure is validated at the example of parameters of a nanoelectrode array biosensor that are precisely known. In addition to a validation of the physical model and Bayesian inversion, the numerical results here show how the procedure predicts the accuracy of a sensor.

4.1. Estimation of the permittivity of the stern layer

The first example is Bayesian inversion for the relative permittivity of the Stern layer for the 1D-system of Fig. 1(b–c). The electrolyte we consider is 100 mM NaCl in water.

As discussed in Sect. 3, an MCMC algorithm determines parameters Q given measurements M and a physical model g. In this case, the unknown parameter is $q = \varepsilon_{r,\text{Stern}}$, while the physical model function g is $g(q) = g(\varepsilon_{r,\text{Stern}}) = C_{\text{enbios,AC}}(\varepsilon_{r,\text{Stern}})$. The measurement is taken from the solution of the analytical model for the 1D-system in Eq. (6) prescribing the specific value $\varepsilon_{r,\text{Stern}} = 7$ for the Stern layer permittivity, i.e., the measurements are $m = C_{\text{a.m.}}(\varepsilon_{r,\text{Stern}} = 7)$. Noise with the known variance σ_L is also added to this synthetic measurement.

To summarize, the model $g(q) = C_{\text{enbios,AC}}(\varepsilon_{r,\text{Stern}})$ will be fitted using the measurement $m = C_{\text{a.m.}}(\varepsilon_{r,\text{Stern}} = 7)$ to estimate the parameter $q = \varepsilon_{r,\text{Stern}}$. Since the true parameter value for the experiment is known *a priori* in this case (as the "experiment" here is an analytical expression computed with a specific value for the parameter), this example serves as a validation for the estimation methodology.

Two frequencies f of the AC signal will be considered separately: $f = 100\,\text{kHz}$ and $f = 1\,\text{GHz}$ corresponding to two distinct values of $m = C_{\text{a.m.}}$ and $g = C_{\text{enbios,AC}}$, which are both frequency-dependent as seen in Eq. (6) and Fig. 2.

4.1.1. MH algorithm with uniform distribution as prior and proposal

First, we assume that there is no a priori knowledge about where in a reasonably large interval the true parameter values (the dielectric permittivity) lies. Therefore, we use a uniform distribution as the prior distribution. The proposal distribution used for sampling is also a uniform distribution.[1] This leads to the following detailed setup for the numerical calculations.

1. The prior distribution is

$$\pi_0(q) := \frac{1}{q_{\max} - q_{\min}} \chi_{[q_{\min}, q_{\max}]}(q),$$

[1] Note that a uniform distribution does in principle not satisfy the irreducibility condition mentioned at the end of Sect. 3.2 for the whole space $\mathbb{R}^d$ because it is bounded. However, in these examples, the irreducibility condition is satisfied since we know *a priori* where the true solution is and we choose an interval large enough to include the true solution. The consequences of selecting a bounded distribution that does not include the true solution will also be discussed in Fig. 10 (right).

Table 1
Set of 14 MCMC simulations with the maxima of the 14 posterior distributions, obtained by means of a kernel density estimator, and the mean value of the Markov chain.

$q = \varepsilon_{r,Stern}$ from KDE posterior max	$q = \varepsilon_{r,Stern}$ from MCMC mean
7.0	7.108 984
7.1	7.108 339
6.9	7.105 623
6.9	7.103 781
7.1	7.106 933
6.8	7.108 801
7.0	7.107 482
7.1	7.110 569
7.0	7.107 669
7.1	7.106 030
7.1	7.108 881
7.1	7.108 628
6.8	7.108 983
7.0	7.108 230

where $\chi_{[q_{\min},q_{\max}]}$ is the characteristic function of the interval $[q_{\min}, q_{\max}]$. We set $q_{\min} := 2$ and $q_{\max} := 20$.

2. The likelihood function $\pi(m|q)$ of a measurement m given a parameter value q is a normal distribution centered around the model response $g(q)$, i.e.,

$$\pi(m|q) := \frac{1}{\sqrt{2\pi\sigma_L^2}} \exp\left(-\frac{(m - g(q))^2}{2\sigma_L^2}\right), \tag{10}$$

where m represents the measurement and $g(q)$ is the model. This likelihood function is consistent with the statistical model and a mean-zero error.

3. The proposal distribution is defined as the uniform distribution

$$J(q \to q') := \frac{1}{q_{\max} - q_{\min}} \chi_{[q_{\min},q_{\max}]}(q) = J(q' \to q),$$

which is symmetric.

4. Therefore the acceptance ratio simplifies to

$$\alpha = \min\left(1, \exp\left(\frac{(m - g(q_{k-1}))^2 - (m - g(q^*))^2}{2\sigma_L^2}\right)\right).$$

For the first frequency point $f = 100\,\text{kHz}$ under test, we sample $g(q)$ via MCMC over the discrete parameter points $\Omega_q = [2{:}0.1{:}20]$ of the uniform distribution. For $\sigma_L := 0.01\,\text{F/m}^2$, the data in Table 1 are obtained, where each row represents one of 14 different MCMC simulations. The first column reports the parameter value (permittivity of the Stern layer) for which the posterior distribution obtained by means of a KDE has a maximum. The second column shows the mean values estimated using $N_{\text{samples}} = 10^6$. We observe the consistency of the mean value ≈ 7.1 obtained for the different 14 MCMC simulations, and that both the KDE posterior maxima and the MCMC means are close to $q = \varepsilon_{r,\text{Stern}} = 7$. The best agreement between the measurement $m = C_{\text{a.m.}}$ and the model $g(q) = C_{\text{enbios,AC}}(\varepsilon_{r,\text{Stern}})$ is obtained precisely for $q = \varepsilon_{r,\text{Stern}} = 7$ (corresponding to $C_{\text{enbios,AC}} = 0.091921\,\text{F/m}^2$). Fig. 3 shows the prior distribution and the posterior distribution with its maximum close to 7. To check convergence, Fig. 4 (left) shows the associated normalized autocovariance function (autocorrelation) and Fig. 4 (right) the respective ergodic mean, which stabilizes around 7. We used a burn-in period of 10^4, and the acceptance ratio corresponding to this run was 0.181 969. The convergence of more complex extraction procedures is discussed in Section 5.3.1.

4.1.2. MH algorithm with normal distributions as prior and proposal

In this second case, we use normal distributions as prior and proposal distributions. The details of the algorithm are the following.

1. The prior distribution

$$\pi_0(q) := \exp(-(q - \hat{q})^2/2\sigma_{\text{prior}}^2)/\sqrt{2\pi\sigma_{\text{prior}}^2}$$

is centered around a chosen value $\hat{q}$ that represents initial information.

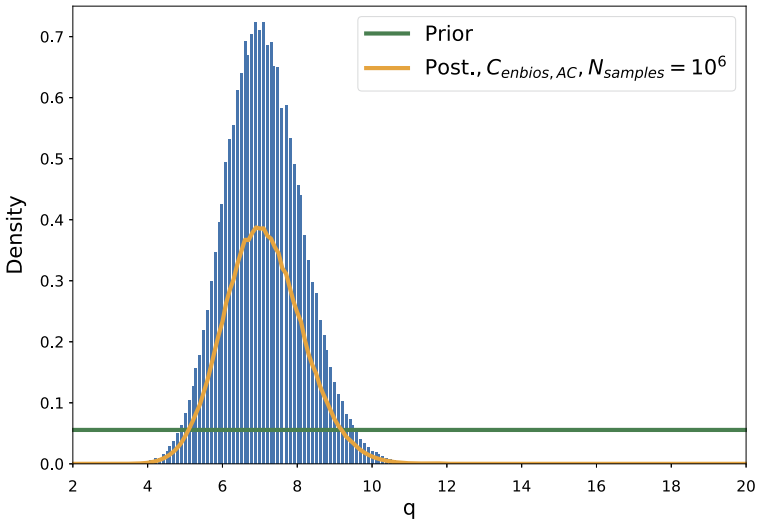

Fig. 3. Prior distribution (green) and posterior distribution (orange) drawn together with its normalized histogram (blue) for $g(q) = C_{\text{enbios,AC}}(\varepsilon_{r,\text{Stern}})$ using $N_{\text{samples}} = 10^6$ samples. Electrolyte: 100 mM NaCl in water. (For interpretation of the colors in the figure(s), the reader is referred to the web version of this article.)

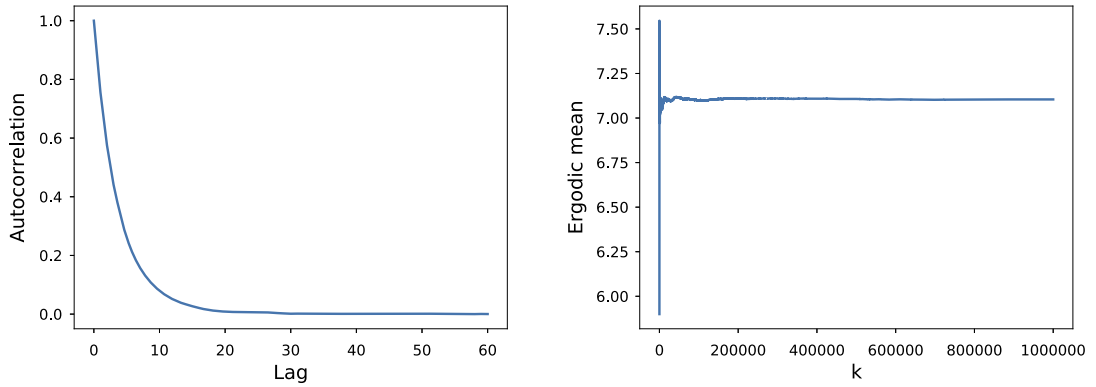

Fig. 4. Left: autocorrelation function for the Markov chain generated by the MCMC algorithm using a uniform distribution as the prior. Right: corresponding ergodic mean.

2. The likelihood function is again (10).
3. The proposal distribution is defined as the normal distribution

$$J(q \to q') := \frac{1}{\sqrt{2\pi\sigma^2_{\text{proposal}}}} \exp\left(-\frac{(q-q')^2}{2\sigma^2_{\text{proposal}}}\right) = J(q' \to q),$$

which is symmetric.

4. The acceptance ratio now simplifies to

$$\alpha = \min\left(1, \exp\left(\frac{(m - g(q_{k-1}))^2 - (m - g(q^*))^2}{2\sigma_L^2} + \frac{(q_{k-1} - \hat{q})^2 - (q^* - \hat{q})^2}{2\sigma^2_{\text{prior}}}\right)\right).$$

Since the proposal function is symmetric, i.e., $J(q \to q') = J(q' \to q)$, the related terms in the acceptance ratio α can be simplified and only the terms related to the prior and the likelihood distributions remain. Moreover, since we have chosen normal distributions for the latter two functions, the argument of the exponential in the acceptance ratio represents a least-squares competition between the parameter related terms and the measurement related terms, or more precisely between the confidence we have in the parameter value $\hat{q}$ in the prior and in the measurement.

The variance σ_L^2 in the likelihood function is given by the measurement error and can be found from the measurements in practice. It will be further discussed in later sections.

Table 2
Extracted $q = \varepsilon_{r,\text{Stern}}$ computed as the mean of the Markov-chain values for various settings. The parameters here are $\hat{q} = 7.2$, $\sigma_{prior} = 0.3$, $\sigma_L = 0.001\,\text{F/m}^2$.

Measurement m	Physical model $g(q)$	N_{samples}	Parameter q (MH mean)
$C_{\text{a.m.}}$	$C_{\text{enbios,AC}}$	10^4	7.037 510
$C_{\text{a.m.}}$	$C_{\text{enbios,AC}}$	10^5	7.015 863
$C_{\text{enbios,AC}}$	$C_{\text{a.m.}}$	10^4	7.026 537
$C_{\text{enbios,AC}}$	$C_{\text{a.m.}}$	10^5	7.022 535
$C_{\text{enbios,AC}}$	$C_{\text{a.m.}}$	10^6	7.018 337

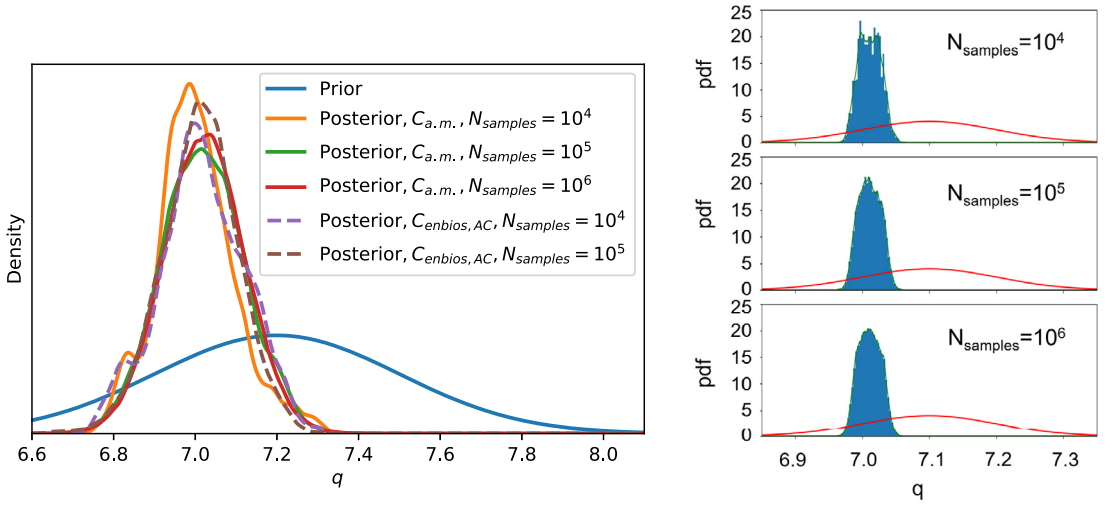

Fig. 5. Prior (normal distribution) and posterior distributions corresponding to a frequency of $f = 100\,\text{kHz}$. Left: comparison between the two approaches (model $g = C_{\text{enbios,AC}}$ and model $g = C_{\text{a.m.}}$) for different values of N_{samples}. The parameters in the algorithm are $\hat{q} = 7.2$, $\sigma_{\text{prior}} = 0.3$, $\sigma_L = 0.001\,\text{F/m}^2$. Right: analyses for the model $g = C_{\text{a.m.}}$ also showing posterior histograms. The parameters in the algorithm are $\hat{q} = 7.1$, $\sigma_{\text{prior}} = 0.1$, $\sigma_{\text{proposal}} = 0.1$, $\sigma_L = 10^{-4}\,\text{F/m}^2$.

In order to further check the properties of reconstructions, we now consider the parameter estimation for the system of Fig. 1(b–c) using information from two different frequencies (100 kHz and 1 GHz) and focus on: (1) how the shape of the posterior density is improved compared to the first example, (2) how the convergence of the mean of the density to the true value is achieved using more samples, and (3) the effects of the choice of the prior distribution.

To obtain more samples, here we also consider the opposite approach compared to the numerical results reported above. Now we use ENBIOS to provide the experimental values and use the analytical model of Eq. (6) as the physical model for sampling. With this approach, a much larger number of samples, namely up to $N_{\text{samples}} = 10^6$, can be easily achieved in a short time. In the following, we will show results for both of the approaches, i.e.,

- measurement $m = C_{\text{enbios,AC}}$ (slow) and physical model $g(q) = C_{\text{a.m.}}(\varepsilon_{r,\text{Stern}})$ (fast) and
- measurement $m = C_{\text{a.m.}}$ (fast) and physical model $g(q) = C_{\text{enbios,AC}}(\varepsilon_{r,\text{Stern}})$ (slow)

with the true parameter value $q = \varepsilon_{r,\text{Stern}} = 7$.

Frequency 100 kHz. In this case we observed that the Bayesian MCMC code correctly identifies the true value of $q = \varepsilon_{r,\text{Stern}} = 7$ using $\sigma_L = 0.001\,\text{F/m}^2$ for $N_{\text{samples}} \in \{10^4, 10^5, 10^6\}$. Larger values of the measurement variance σ_L, e.g. $\sigma_L = 0.01\,\text{F/m}^2$ yield instead $q = 7.2$ for $N_{\text{samples}} \in \{10^4, 10^5, 10^6\}$ samples (not shown). This was consistently found for both kinds of runs, using measurements $m = C_{\text{a.m.}}$ and the model $g = C_{\text{enbios,AC}}$ or using measurements $m = C_{\text{enbios,AC}}$ and the model $g = C_{\text{a.m.}}$. This behavior is of course expected, since a smaller measurement variance or error enables better reconstructions.

Table 2 lists the information obtained from both runs. In all results in this table, the standard deviation of the error in the likelihood function is $\sigma_L = 0.001\,\text{F/m}^2$. The estimated parameter values are close to the true value and the dependence on the number of samples is small.

Fig. 5 (left) shows the corresponding posterior and prior distributions. For the case where the model is $g = C_{\text{a.m.}}$, the posterior PDF becomes smoother with increasing N_{samples}. Furthermore, N_{samples} has to be large enough (10^5 or greater) to pass the burn-in period [3] and provide give a good estimate of the mean. For the sake of comparison, Fig. 5 (left) also shows curves for the other case where the model is $g = C_{\text{enbios,AC}}(\varepsilon_{r,\text{Stern}})$.

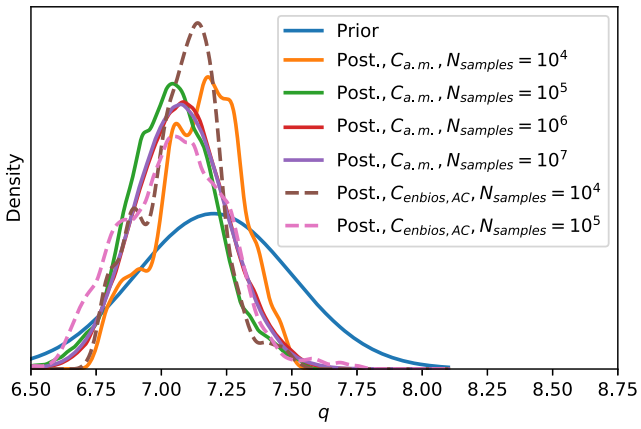

Fig. 6. Prior (normal distribution) and posterior distributions using the model $g(q) = C_{\text{enbios,AC}}$ (two dashed lines) and using the model $g(q) = C_{\text{a.m.}}$ (four solid lines). The frequency is $f = 1\,\text{GHz}$. The parameters in the algorithm are $\hat{q} = 7.2$, $\sigma_{\text{prior}} = 0.3$, and $\sigma_L = 10^{-5}\,\text{F/m}^2$.

Frequency 1 GHz. We consider now a signal frequency in the GHz range, which is a relevant limit case of high frequency detection not yet achieved in current technology. The measured capacitances are different, but the same extraction procedure should deliver the same parameter value.

We start with a prior equal to a normal distribution centered around 7.2 and with standard deviation of 0.3. Again, the Bayesian inversion was performed both using the output of ENBIOS as the experiment $m = C_{\text{enbios,AC}}$ and the analytical model of Eq. (6) as the physical model $g = C_{\text{a.m.}}$ and vice versa.

Fig. 6 shows superposed plots of the posterior and prior distributions for different values of $N_{\text{samples}} = 10^n$.

It is possible to identify the true permittivity value corresponding to a given capacitance measurement $m = C_{\text{enbios,AC}}(\varepsilon_{r,\text{Stern}} = 7) = 6.4070 \times 10^{-3}\text{F/m}^2$ using the model $g = C_{\text{a.m.}}$ with the standard deviation $\sigma_L = 10^{-5}$ F/m^2 of the measurements. A ten times larger value of σ_L yields a parameter value of about 7.2, increasing the error in the estimation (not shown). An increase in the number of samples, e.g., from $N_{\text{samples}} = 10^4$ to $N_{\text{samples}} = 10^5$ smooths the shape of the posterior distribution, which becomes more and more similar to a normal distribution centered around the true value of $\varepsilon_{r,\text{Stern}} = 7.0$ as σ_L decreases.

4.1.3. MH study with normals using priors distant from the solution

To further demonstrate the capability of the algorithm to converge to the expected value, we run the extractions with prior (normal) distributions located far away from the exact solution. This has been done for the $f = 100$ kHz case, keeping all other extraction parameters equal to the extractions of Fig. 5. This analysis demonstrates the influence of the initial guess for the parameter value (via the mean of the prior) on the subsequent posterior distribution attained.

Since the true value of the permittivity parameter is $q = 7$, we used two different prior means: $\hat{q} = 20$ (which is within the limits of the possibly expected values for the permittivity of the Stern layer) and $\hat{q} = 40$ (a permittivity far outside the range of reasonably expected values, essentially a bad guess). Fig. 7 shows the resulting posterior distributions obtained (orange curves, centered around 8.56 for the prior around $\hat{q} = 20$, and centered around 12.7 for the prior around $\hat{q} = 40$) with $N_{samples} = 10^6$. After the first iteration, a Gaussian fit is performed on these posterior distributions to generate a new prior, and the extraction is repeated 4 subsequent times. Fig. 7 shows the convergence of these posterior distributions towards the actual value of 7 for the parameter, arriving to a neighborhood close to the solution (for the $\hat{q} = 20$ case, obtaining a posterior around 7.27, and for the $\hat{q} = 40$ case obtaining a posterior around 7.51). These results illustrate the ability of the iterative algorithm to converge to the expected value in spite of significant offsets with respect to the initial guess.

4.2. Simultaneous estimation of the permittivity of the stern layer and the ionic strength for the 1D system

Having validated the method and its implementation on single-parameter problems, we now use the MCMC technique to carry out simultaneous Bayesian inversion of two parameters, namely the relative permittivity $\varepsilon_{r,\text{Stern}}$ of the Stern layer (nominally still equal to 7) and the ionic strength of the NaCl electrolyte (Na^+ and Cl^- molarity $n^{\infty}_{0,Na^+} = n^{\infty}_{0,Cl^-} = n^{\infty}_0$, nominally equal to 0.1 M). In other words, the parameter vector to be identified is $q = [q_1, q_2] = [\varepsilon_{r,\text{Stern}},\ n^{\infty}_0]$.

As before, we will perform analyses considering the two frequencies $f_{\text{low}} := 100\,\text{kHz}$ and $f_{\text{high}} = 1\,\text{GHz}$. Compared to the previous cases, here we rely on existing data, demonstrating that a previously generated look-up table of model data can also be used. Furthermore, we will use more than a single measurement, thus mimicking more realistic conditions.

To this end, we run ENBIOS simulations to generate a non-regular grid of measurements $C_{\text{enbios,AC}}$ in the $(q_1, q_2) = (\varepsilon_{r,\text{Stern}},\ n^{\infty}_0)$ plane. A total of 10^5 grid points were generated, each one with its associated low and high frequency capacitance values, namely $C^{\text{low}}_{\text{enbios,AC}} = C_{\text{enbios,AC}}(f = 100\,\text{kHz})$ and $C^{\text{high}}_{\text{enbios,AC}} = C_{\text{enbios,AC}}(f = 1\,\text{GHz})$. The sample points are

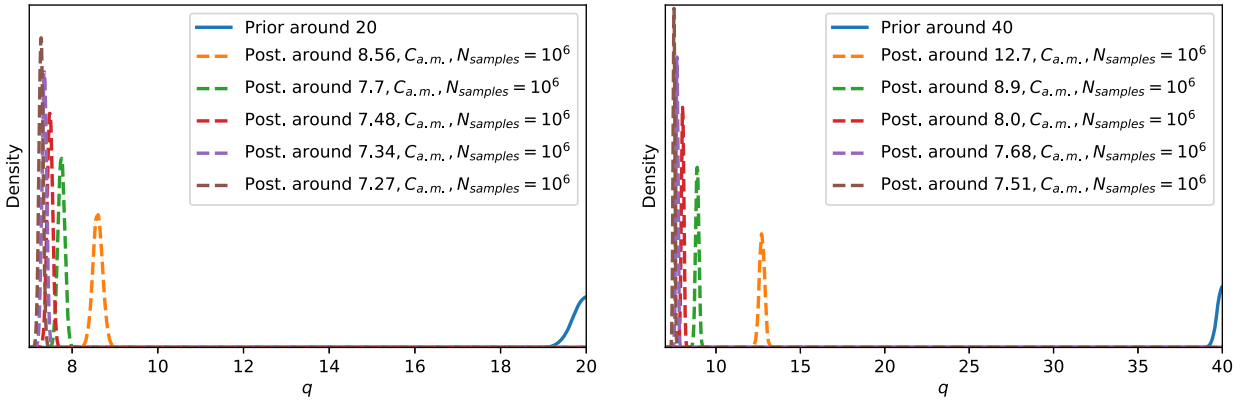

Fig. 7. Left: prior (normal around 20 in solid line) and subsequent iterated posterior (dashed lines) distributions using the model $g(q) = C_{\text{a.m.}}$. The frequency is $f = 100\,\text{kHz}$. The parameters in the algorithm are $\sigma_{\text{prior}} = 0.3$, $\sigma_L = 0.001\,\text{F/m}^2$, and $\hat{q} = 20$ for the initial prior distribution. Right: same as left, for an initial prior centered around $\hat{q} = 40$.

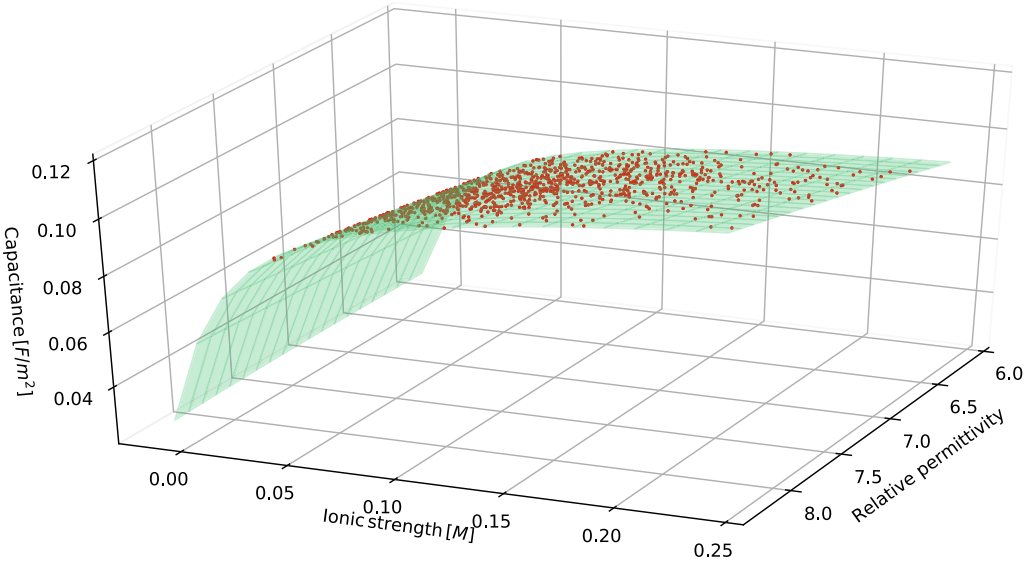

Fig. 8. Polynomial approximation (green) of a randomly selected subset of the simulated points (red).

generated randomly, centered around $(\varepsilon_{r,\text{Stern}}, n_0^\infty) = (7.2, 0.1\,\text{M})$ and the analysis considers each frequency value separately. To be able to evaluate the model function on the whole domain, a polynomial of degree 10 is used to approximate the dataset globally, whereby the coefficients are calculated by minimizing the sum of the squared errors between the simulated capacitances at the grid points and the evaluated polynomial. With a polynomial of degree 10, sufficient precision in the global approximation is achieved (about 1%). The polynomial chosen as an approximation of a randomly selected subset of the simulated points is illustrated in Fig. 8.

As a result, two models $g(q) = C^{\text{low}}_{\text{enbios,AC}}(\varepsilon_{r,\text{Stern}}, n_0^\infty) \colon \mathbb{R}^2 \mapsto \mathbb{R}$ and $g(q) = C^{\text{high}}_{\text{enbios,AC}}(\varepsilon_{r,\text{Stern}}, n_0^\infty) \colon \mathbb{R}^2 \mapsto \mathbb{R}$ are obtained for the low and high frequency data, respectively.

For each frequency of analysis, we rely again on the analytical model of Eq. (6) for artificial measurements, namely $m = C^{\text{low}}_{\text{a.m.}} = C_{\text{a.m.}}(f = 100\,\text{kHz})$ or $m = C^{\text{high}}_{\text{a.m.}} = C_{\text{a.m.}}(f = 1\,\text{GHz})$. Differently from the previous sections, here we do not consider only a single measurement. Instead, $N_m = 10$ distinct artificial measurements are generated for both the low and the high frequency case by taking 10 samples from a normal distribution centered around the nominal values of the parameters, namely $m \sim N(\mu_m, \sigma_m)$, where the mean values are $\mu_m = C^{\text{low}}_{\text{a.m.}}(7.2, 0.1) = 0.0938\,\text{F/m}^2$ or $\mu_m = C^{\text{high}}_{\text{a.m.}}(7.2, 0.1) = 0.0064\,\text{F/m}^2$ and the standard deviations are $\sigma_{\text{low}} = 0.0007\,\text{F/m}^2$ and $\sigma_{\text{high}} = 4.735 \cdot 10^{-5}\,\text{F/m}^2$ for the low and high frequency case, respectively. As a consequence, we can write $m \colon \mathbb{R}^{N_m} \mapsto \mathbb{R}$.

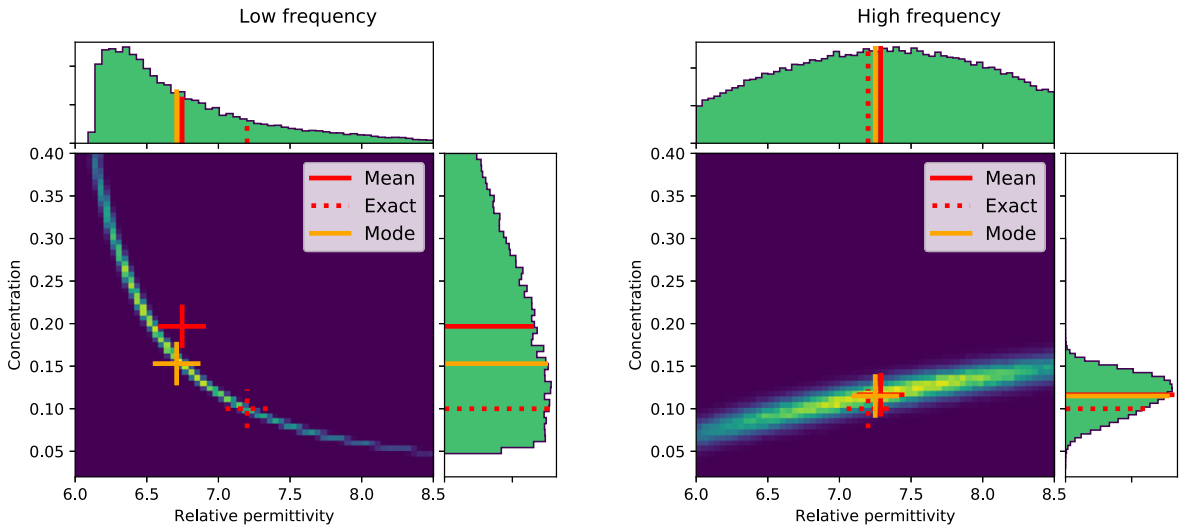

Fig. 9. Two-dimensional histograms of posterior distributions based on $N_{\text{samples}} = 10^6$ and histograms of the marginal posterior distributions for $f = 100\,\text{kHz}$ (left) and $f = 1\,\text{GHz}$ (right). The mean value and the mode of the estimated posterior as well as the "exact" value $q = (\varepsilon_{r,\text{Stern}}, n_0^\infty) = (7.2, 0.1\,\text{M})$ are shown. The range of the colored map coincides with the support of the prior distribution. $C_{\text{enbios,AC}}$ is used for the model, and $C_{\text{a.m.}}$ as artificial measurement.

The likelihood function is

$$\pi(m|q) = (2\pi\sigma_L^2)^{-N_m/2} \exp\left(\sum_{i=1}^{N_m} \frac{(m_i - g(q))^2}{2\sigma_L^2}\right), \tag{11}$$

where the corresponding standard deviation is set to $\sigma_L = \sigma_{\text{low}}$ or $\sigma_L = \sigma_{\text{high}}$ for the low and high frequency case, respectively. We used a uniform distribution in the domain $q_1 \times q_2 = \varepsilon_{r,\text{Stern}} \times n_0^\infty = [6, 8.5] \times [0.02\,\text{M}, 0.4\,\text{M}]$ as the prior distribution. Again, the proposal distribution is a normal distribution.

Fig. 9 shows the two-dimensional histograms of the posterior distributions based on $N_{\text{samples}} = 10^6$. ENBIOS simulations were used for this analysis, with artificial measurements based on the analytical model. The shapes of the distributions suggest remarkably different behaviors at the two different frequencies $g = C^{\text{low}}_{\text{enbios,AC}}$ and $g = C^{\text{high}}_{\text{enbios,AC}}$. This is consistent with expectations from the physical behavior of the system. In fact, at high frequency the Stern and the diffusion layer capacitances are close to short circuits for the AC signal and the relative permittivity $\varepsilon_{r,\text{Stern}}$ has a modest influence on the observable regardless of the electrolyte ionic strength. To extract single values, alternative possibilities are to select the mean value or the mode from on two-dimensional histogram of the posterior distribution. Both of these values are highlighted in Fig. 9.

Fig. 9 demonstrates that a correct determination of the parameters is more difficult at a low frequency, where the covariance matrix is anisotropic. In addition, various parameters yield the same model response which makes it more difficult to reconstruct the parameters. This underlines the advantage of being able to perform parameter extractions at different frequencies: each parameter is easier to estimate at a different frequency, thus a multi-frequency multi-parameter extraction reduces the estimation uncertainty. Thus, multi-frequency operation is an important feature of this sensor platform.

The MCMC run for one frequency with 10^6 samples took only about 33 seconds due to the approximation of the observation function with a polynomial. Most of the computational work is due to the evaluations of the physical model.

5. Estimation of nanoelectrode radii in a sensor array (3D system)

In the previous Sect. 4, we have validated the MCMC methodology to determine the values of physical parameters in nanoelectrode sensors. By means of numerical simulations and analytical expressions, we have demonstrated that the extracted parameters are consistent with the a priori known true values.

Here we set the goal of using MCMC estimation procedures to determine the radii of the nanoelectrodes of the real-world sensor. To this end, we use experiments at controlled temperature $T = 295\,\text{K}$ in IPA ($C_{\text{exp,IPA}}$) and air ($C_{\text{exp,air}}$), which both show a smooth dependency between the experimental capacitance and the nanoelectrode radius. Air and IPA environments can be described by frequency independent capacitance values, because in the absence of ions the spreading resistance $1/G_E$ is very large.

Since in the real biosensor array an unknown parasitic capacitance C_P, essentially independent of nanoelectrode size, adds in parallel to the system (see Fig. 1, c), we use the difference between the response of the sensor to IPA and air, namely $m = \Delta C_{\text{exp}} = C^{\text{IPA}}_{\text{exp}} - C^{\text{air}}_{\text{exp}}$ as experimental measurements in the following. By doing so, we remove the dependency

on the parasitic C_P from our observable. The variance σ_L of the measurement is estimated from the noisy data and will be used in the estimation procedures. In the following, we restrict the analyses to a small sub-array of 71×31 nanoelectrodes within the full 256×256 nanoelectrodes array in order to prune evident outliers.

Regarding the physical model for the MCMC estimation, the complex three-dimensional distribution of electric field flowlines in the array cannot be easily described in purely analytical forms; thus, using data from full-3D ENBIOS numerical simulations is mandatory. Hence, we will use our new switching capacitance model $C_{\text{enbios,F}}$ as the physical model (see Sect. 2.3). By analogy with the measurement quantity, the observable quantity for the model is the capacitance difference between IPA and air, namely $g = \Delta C_{\text{enbios,F}} = C^{\text{IPA}}_{\text{enbios,F}} - C^{\text{air}}_{\text{enbios,F}}$.

The estimation process is split into multiple consecutive steps.

5.1. Measurement protocol

Measurements have been performed with the CMOS biosensor platform described in [11] in our Nanoelectronics Lab in Udine (Italy). Calibration measurements in dry are run first to estimate the electrical parameters of the transistors of the readout circuit needed in frequency calibration procedures (more details about calibration measurements can be found in [11]). The temperature controller is configured to maintain a stable chip temperature of 295 K during calibrations and experiments, and liquids (IPA) are pumped in the fluidic chamber at a controlled rate of 50 µL/min. The first 10 minutes of each experiment are discarded to guarantee a stable temperature of the control electronics as well.

Each nanoelectrode is alternatively charged and discharged at a controlled switching frequency f_s; the average charging current is integrated to obtain the capacitance information. To improve the signal-to-noise ratio, data-accumulations are performed on-chip.

The measurements reported in this work have been performed either at fixed $f_s = 50\,\text{MHz}$ or by sweeping f_s in 27 log-spaced points between 1 MHz and 70 MHz. The number of charging/discharging cycles for each electrode is 1088, and 9 data accumulations have been applied. The post-measurement calibration of [11] is applied on each measurement frame to correct for capacitance-dependent voltage shifts.

The average capacitance of each electrode and the standard deviation (in air and in IPA) are extracted off-chip from time-averages over 2 minutes long time series.

5.2. One parameter estimation of the average nanoelectrode radius

The first step aims at estimating the ensemble average of the nanoelectrodes radii in the array, i.e., the *mean* radius r_{av}. Experiments in air and IPA at 50 MHz give a mean experimental $\Delta C^{\text{av}}_{\text{exp}} = 32\,\text{aF}$ with an uncertainty of 1 aF (one standard deviation). The ENBIOS simulations have been run on a 7×7 array of electrodes at 50 MHz extracting the capacitance of the central electrode. The chosen size of the array is large enough that the central electrode capacitance is only modestly affected by the domain boundaries. We indicate by $r^i_{\text{enbios,el}}$ the radius of the i-th electrode of the simulated array ($i \in [1, 49]$). To sample the model function, all the electrodes of every simulation had the same common size $r^i_{\text{enbios,el}} = r_{\text{av}}$ for all i, and we swept this common value between 70 nm and 110 nm.

Based on the average experimental response $m = \Delta C^{\text{av}}_{\text{exp}}$ of the array and on the ENBIOS model $q = r_{\text{av}}$, $g(q) = \Delta C_{\text{enbios,F}}(r_{\text{av}})$ in which we vary the size of all the electrodes at the same time, we then apply our MCMC analysis to determine the posterior PDF of r_{av}.

Starting with a uniform distribution on the interval [70 nm, 110 nm] (which is large enough to include the true average radius, which we expect to be close to 90 nm [11]), we run $N_{\text{samples}} = 10\,000$ iterations in the Metropolis-Hastings algorithm. The proposal distribution, here and in the rest of the paper, is again a normal distribution. Fig. 10 (left) shows the prior and posterior PDFs. An estimation of $r_{\text{av}} = 86.5\,\text{nm}$ is obtained. The impact of a possibly wrong choice of this interval swept ([70 nm, 80 nm] that does not contain the true value is shown in Fig. 10 (right): the posterior PDF is squeezed against the upper boundary, since convergence to the true value is blocked by the domain limits.

In the following, we take the estimated value $r_{\text{av}} = 86.5\,\text{nm}$ as our initial radius for all of the following MCMC estimations. The simulated value corresponding to r_{av} is $\Delta C_{\text{enbios,F}}(r_{\text{av}}) = 32.42\,\text{aF}$, which confirms our confidence in the estimation since the value is very close to $\Delta C^{\text{av}}_{\text{exp}} = (32 \pm 1)\,\text{aF}$.

5.3. One parameter estimation of individual radii

In the previous section, we have estimated the mean radius of the electrodes based on one measurement $\Delta C^{\text{av}}_{\text{exp}}$ at 50 MHz. The goal now is to estimate the size of individual nanoelectrodes and hence to generate maps of electrode radii. The purpose of the analysis is to verify whether the assumption that radii fluctuations are the dominant source of variability in individual ΔC_{exp} measurements is realistic. Now we estimate one single parameter at a time, namely $r^{i,j}_{\text{el}}$, the radius of an individual nanoelectrode in the 71×31 matrix, where i and j identify the row and column in the array while using ΔC_{exp} data recorded at 27 different frequencies logarithmically spaced from 1 MHz to 70 MHz. Using multi-frequency data is an interesting application of MCMC estimation to real experiments using multi-dimensional measurements.

We run multi-frequency ENBIOS simulations setting all the nanoelectrodes radii at $r_{\text{av}} = 86.5\,\text{nm}$ except for the central electrode of the 7×7 array, whose radius $r^{\text{central}}_{\text{enbios,el}}$ is swept from 70 nm to 110 nm. The model response is then the IPA-air

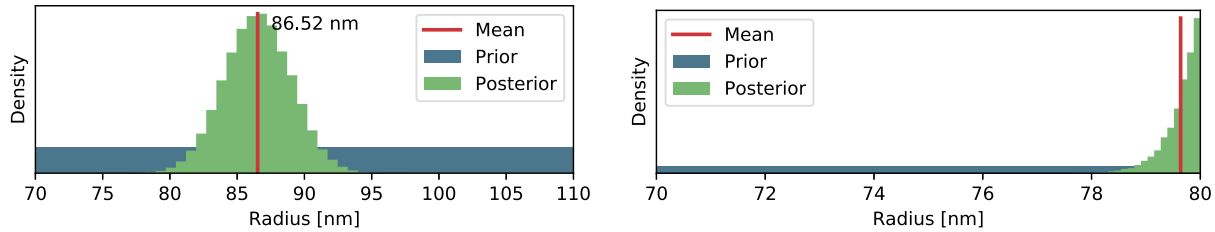

Fig. 10. Histograms of the uniform prior and posterior distributions after $N_{\text{samples}} = 10\,000$ iterations of the Metropolis-Hastings algorithm. Left: the domain [70 nm, 110 nm] of the parameter and the extracted $r_{\text{av}} = 86.5$ nm is marked. Right: the domain [70 nm, 80 nm] is too small and therefore the samples accumulate at the right boundary emphasizing the unsuitable choice of the domain.

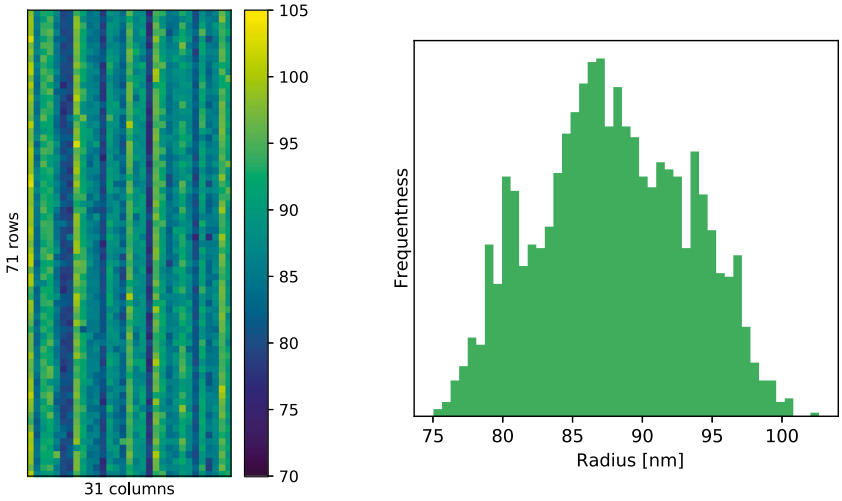

Fig. 11. Left: estimated radii $r_{\text{el}}^{i,j}$ for all the electrodes using data collected at 27 frequencies. In the ENBIOS simulations, we swept the size of the central electrode only keeping all the others at the r_{av} value estimated in Sect. 5.2. Right: distribution of the extracted $r_{\text{el}}^{i,j}$ values.

capacitance variation at this central electrode of the simulated array, i.e., $g = \Delta C_{\text{enbios,F}}(r_{\text{enbios,el}}^{\text{central}})$. As for the experiments, we performed the individual extraction of the radii for all the 71×31 electrodes, in each independent iteration using $m = \Delta C_{\text{exp}}^{i,j}$, where $\Delta C_{\text{exp}}^{i,j}$ is the experimental value recorded at the electrode in row i and column j of the 71×31 subarray.

Running the MCMC analysis with $N_{\text{samples}} = 5000$ for each electrode and extracting the mean values of the resulting posterior distributions, we obtained a 71×31 array of estimated $r_{\text{el}}^{i,j}$ values as reported in colormap form in Fig. 11. Surprisingly, the results show column-wise patterns and a large spread of the individual values (i.e., a broad posterior distribution), which will be explained in more detail in the following.

5.3.1. Convergence and autocorrelation function

To test the statistical convergence of the generated Markov chains, we studied the correlation between the samples and calculated the autocorrelation function (ACF) defined by

$$\text{ACF}(N,t) := \frac{\sum_{k=1}^{N-t}(q_k - \overline{q})(q_{k+t} - \overline{q})}{\sum_{k=1}^{N}(q_k - \overline{q})^2}, \tag{12}$$

where q_k and $\overline{q}$ are the k-th state of the Markov chain and the sample mean, respectively. This formula reflects the idea of computing the correlation between the subchains of length N with lag t. The numerator of Eq. (12) is an estimate of the autocovariance and the denominator is an estimate of the variance of the chain in order to normalize the output. Low autocorrelation means that samples are independent and mixing in the chain is good. Fig. 12 shows the autocorrelation functions for the Markov chains of the parameter of interest, which have been generated by the MCMC algorithm and illustrates their convergence.

5.4. Nine parameter estimation of individual radii

The estimation in Sect. 5.3 assumes that all nanoelectrodes except the central one have radius $r_{\text{enbios,el}} = r_{\text{av}}$. Thus, it neglects the influence that differently sized neighbor electrodes may have on the capacitance of the central electrode. This

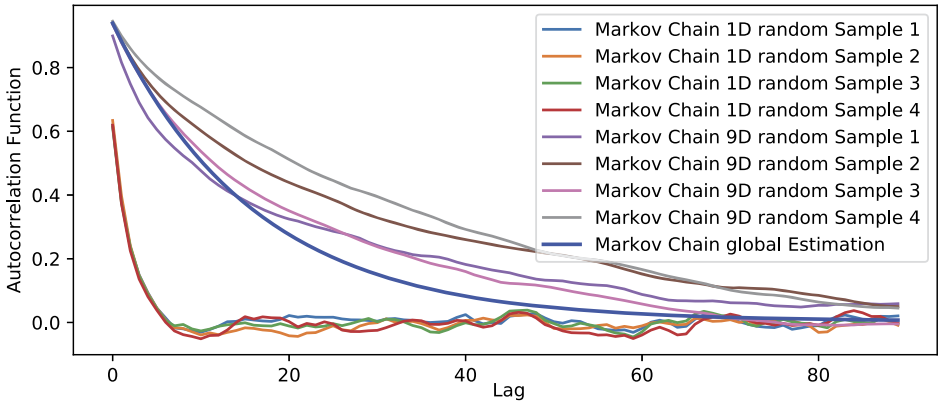

Fig. 12. Autocorrelation function for the generated Markov chains in the global, local 1D, and local 9D estimations.

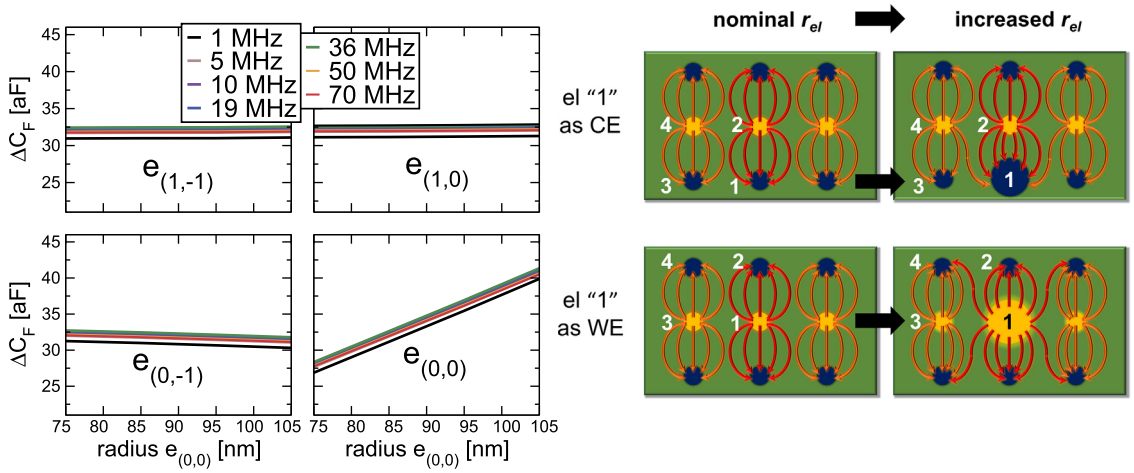

Fig. 13. Left: response of simulated capacitance of four neighboring electrodes at different frequencies. The radius of electrode number 1 varies between 70 nm and 110 nm, while the other radii remain fixed. Right: sketch of the configuration of current-flux lines comparing a group of electrodes at nominal dimension (left) to a bigger electrode number 1 (right). Due to the row-wise excitation, we measure the electrodes on the row 4–2, electrode 1 is a counter electrode; when we measure the electrodes on the row 3–1, electrode 1 is a working electrode.

relation may be important in view of the difference in x- and y-pitch of the electrodes and the large spread of extracted values in Fig. 11.

Fig. 13 (left) explores this relation by showing the simulated ENBIOS capacitance of four neighboring electrodes in a 2×2 subarray of the 7×7 matrix as a function of the size of one of them (electrode #1). The top plots (which measure electrodes 2–4) correspond to electrode #1 being a counter electrode, the bottom plots (measuring electrodes 1–3) when it is a working electrode. The response of electrode #1 increases with the electrode radius, as expected based on simple analytical calculations on an isolated circular disk in a uniform dielectric medium. The response increase of the first neighbor on the same column (electrode #2) is barely visible. In fact, an increase of the size of CE #1 increases the current at WE #2 (a bigger electrode #1 corresponds to shorter path for the current lines, see Fig. 13, top right), but only minimally since other electrodes contribute to sink the current from electrode #1. Similar arguments apply to electrode #4 (top row).

Differently, the response of the first neighbor WE on the same row (electrode #3) decreases. This behavior can be understood looking at Fig. 13 (bottom right) and again recalling that nanoelectrodes are excited row by row (Sect. 2.1). When electrode #1 is active, electrode #3 is active as well. The increased size of electrode #1 partially obstructs the current flowlines originating from the neighbor electrode #3, thus reducing its AC current and capacitance. On top of that, the pitch of the nanoelectrodes array along the x- and y-directions is asymmetrical (600×720 nm); hence, electrodes on the same row affect each other more than neighbor electrodes on the same column do.

This analysis of the model function obtained by ENBIOS simulations elucidates that a relation exists between the size of one nanoelectrode and the capacitance reading at neighbor electrodes especially those along the same row. Hence, a simultaneous estimation of one electrode dimensions considering neighbors as well is desirable for more accurate results.

Consequently, we perform a nine-dimensional Bayesian extraction of the individual electrode radii simultaneously extracting the size of electrodes in small 3×3 subarrays. All other electrodes are kept at the nominal dimension $r_{\text{enbios,el}} = r_{\text{av}}$.

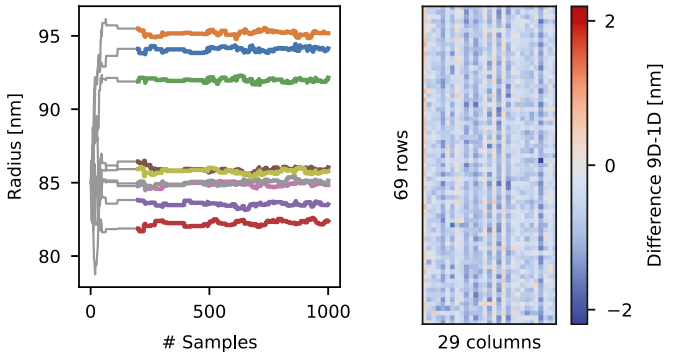

Fig. 14. Left: paths of all nine Markov chains for a 3×3 electrode estimation. The distributions are seen to be stationary after the first 200 samples (thick lines). Right: array color map of the difference $r^{i,j}_{\mathrm{el,9D}} - r^{i,j}_{\mathrm{el}}$ between the nine-dimensional and one-dimensional radius estimates.

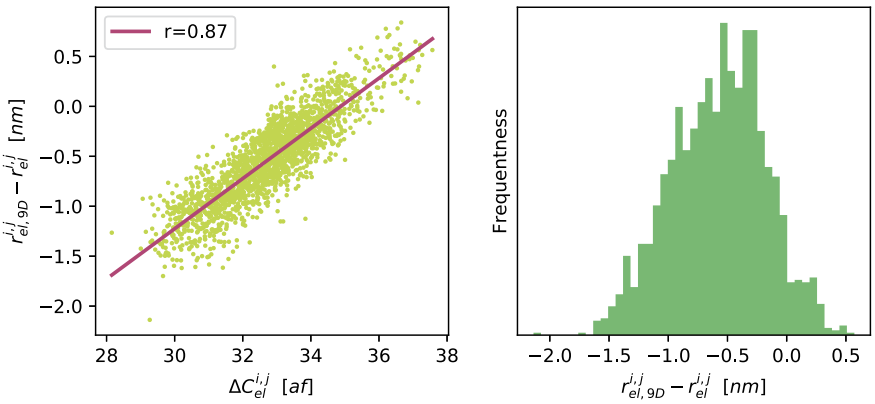

Fig. 15. Left: scatter plot of the change $r^{i,j}_{\mathrm{el,9D}} - r^{i,j}_{\mathrm{el}}$ in estimated electrode radius when moving from 1D to 9D extraction versus nanoelectrode capacitance $\Delta C^{i,j}_{\mathrm{el}}$. Each point corresponds to one electrode. Note that the 9D extraction method yields an even larger radius than the 1D method for large electrodes ($r^{i,j}_{\mathrm{el,9D}} - r^{i,j}_{\mathrm{el}} > 0$) and a smaller one for small electrodes ($r^{i,j}_{\mathrm{el,9D}} - r^{i,j}_{\mathrm{el}} < 0$). Right: corresponding histogram of $r^{i,j}_{\mathrm{el,9D}} - r^{i,j}_{\mathrm{el}}$.

As done previously, the procedure is iterated to generate a map of 69×29 values. By doing so, we take into account the correlation between the size of one electrode and the response at first neighbor ones.

Using the measurements for the 69×29 subarray and implementing a uniform prior distribution on $[70\,\mathrm{nm}, 110\,\mathrm{nm}]$[9] equivalent to the 1D uniform prior used above, we can compare the results of the nine-parameter approach with those obtained with the 1D approach.

We perform simulations of partially overlapping 3×3 arrays, whereby we extract $r^{\mathrm{central}}_{\mathrm{enbios,9D}}$ for the center electrode. This results in $69 \cdot 29 = 2001$ nine-dimensional simulations. To reduce the computational cost, a sample size of 1000 samples for each estimation process has been chosen. We assume that the distributions are stationary after a burn-in period of 200 samples so that we calculate the mean values of these 800 samples as our estimates $r^{i,j}_{\mathrm{el,9D}}$ as shown in Fig. 14 (left).

Fig. 14 (right) shows the array color map of the differences $r^{i,j}_{\mathrm{el,9D}} - r^{i,j}_{\mathrm{el}}$ between the nine-dimensional and the one-dimensional estimations.

The nine-dimensional approach should give more accurate results due to the consideration of the neighboring electrodes. We note that the difference is as large as 2 nm (Fig. 14), which is not negligible in absolute terms for the sake of an accurate extraction, but nevertheless relatively small compared to the large spread of the data in Fig. 11. The 9D extraction method yields an even larger radius than the 1D method for large electrodes ($r^{i,j}_{\mathrm{el,9D}} - r^{i,j}_{\mathrm{el}} > 0$) and a smaller one for small electrodes ($r^{i,j}_{\mathrm{el,9D}} - r^{i,j}_{\mathrm{el}} < 0$), thus effectively increasing the spread of the extracted radii values (Fig. 15). It is also interesting to note that the difference between values extracted by the nine-dimensional and the one-dimensional procedure depends on the mean capacitance of the neighboring working electrodes, consistently with Fig. 13. In fact, if we fix the center electrode but sweep neighbor working electrodes on the same row, we observe a change in the capacitance of the center electrode.

These results suggest that the inter-electrode capacitance relation, while being important for the accuracy of the results, cannot entirely account for the observed spread. In fact, the latter is still large for the production-class technology used in chip fabrication [11], and it is even amplified when moving from the 1D to the simultaneous 9D multi-electrode extraction.

We thus conclude that fluctuations of r_{el} cannot fully explain the variability of our capacitance measures. The residual column-wise pattern suggests that the column readout circuitry could be an important source of variability in this sensor implementation.

6. Discussion and conclusions

In this paper we demonstrated the application of multi-frequency and multi-parameter Bayesian inference to the extraction of electrical and geometrical parameters of nanoscale biosensor platforms. The MCMC methodology was first assessed and validated by means of simulations and analytical models, proving that the extracted parameter values are consistent with the *a-priori* known values. Then, the technique has been applied on a relevant technological test case, namely the estimation of the size of nanoelectrodes of a real nanobiosensor platform. The impact of neighboring electrodes on the size estimation has been evaluated quantitatively.

The extracted radii correctly reproduce experiments by ENBIOS simulations; the column-striped pattern visible in Fig. 11, however, was not corrected by more sophisticated extractions accounting for inter-electrode coupling and the large observed spread of the extracted data is actually increased in the 9D estimation. This suggests that additional (column-sensitive) sources of variability affect the capacitance reading, possibly due to the column-wise architecture of the readout circuits. The detailed investigation of the root cause of this result lies beyond the scope of this contribution.

Acknowledgements

This research was supported in part by the FLAG-ERA CONVERGENCE project via the Italian MIUR and the IUNET Consortium (grant number CONVERGENCE JTC 2016-HESN) and by the FWF (Austrian Science Fund) START Project no. Y660 *PDE Models for Nanotechnology*. P.S. acknowledges partial support by Fondo Sociale Europeo 2007-2013 (POR FSE). The authors thank F. Widdershoven (NXP Semiconductors) and S.G. Lemay (University of Twente) for insightful discussions.

References

[1] Y. Wang, B. Cheng, X. Wang, E. Towie, C. Riddet, A. Brown, S. Amoroso, L. Wang, D. Reid, X. Liu, et al., Variability-aware TCAD based design-technology co-optimization platform for 7 nm node nanowire and beyond, in: IEEE Symposium on VLSI Technology, IEEE, 2016, pp. 1–2.
[2] A. Asenov, S.M. Amoroso, L. Gerrer, F. Adamu-Lema, V.P. Georgiev, X. Wang, TCAD-based design technology co-optimization for variability in nanoscale SOI FinFETs, in: Integrated Nanodevice and Nanosystem Fabrication, Pan Stanford, 2017, pp. 235–272.
[3] R.C. Smith, Uncertainty Quantification: Theory, Implementation, and Applications, vol. 12, SIAM, 2013.
[4] B.V. Rosić, A. Kučerová, J. Sýkora, O. Pajonk, A. Litvinenko, H.G. Matthies, Parameter identification in a probabilistic setting, Eng. Struct. 50 (2013) 179–196, Engineering Structures: Modelling and Computations (special issue IASS-IACM 2012).
[5] E.S. Jackson, W.J. Fitzgerald, Introduction to Bayesian methods for biosensor design, in: Handbook of Biosensors and Biochips, 2008.
[6] A. Papoulis, S.U. Pillai, Probability, Random Variables, and Stochastic Processes, Tata McGraw-Hill Education, 2002.
[7] H.W. Engl, P. Kügler, Nonlinear inverse problems: theoretical aspects and some industrial applications, in: Multidisciplinary Methods for Analysis Optimization and Control of Complex Systems, Springer, 2005, pp. 3–47.
[8] M. Kern, Numerical Methods for Inverse Problems, John Wiley & Sons, 2016.
[9] B. Stadlbauer, L. Taghizadeh, J.M. Escalante, C. Heitzinger, A. Cossettini, L. Selmi, Bayesian estimation for transport equations for nanocapacitors, in: Proc. SIAM Conference on Uncertainty Quantification, UQ 2018, Garden Grove, CA, USA, 2018, pp. 69–70.
[10] A. Cossettini, P. Scarbolo, J.M. Escalante, B. Stadlbauer, N. Muhammad, L. Taghizadeh, C. Heitzinger, L. Selmi, Calibration, compensation, parameter estimation, and uncertainty quantification for nanoelectrode array biosensors, in: Proc. SIAM Conference on Uncertainty Quantification, UQ 2018, Garden Grove, CA, USA, 2018, p. 81.
[11] F. Widdershoven, A. Cossettini, C. Laborde, A. Bandiziol, P.P. van Swinderen, S.G. Lemay, L. Selmi, A CMOS pixelated nanocapacitor biosensor platform for high-frequency impedance spectroscopy and imaging, IEEE Trans. Biomed. Circuits Syst. 12 (2018) 1369–1382.
[12] F. Widdershoven, et al., CMOS biosensor platform, Proc. IEDM (2010) 816–819.
[13] C. Laborde, F. Pittino, H. Verhoeven, S. Lemay, L. Selmi, M. Jongsma, F. Widdershoven, Real-time imaging of microparticles and living cells with CMOS nanocapacitor arrays, Nat. Nanotechnol. 10 (2015) 791–795.
[14] S.G. Lemay, C. Laborde, C. Renault, A. Cossettini, L. Selmi, F.P. Widdershoven, High-frequency nanocapacitor arrays: concept, recent developments, and outlook, Acc. Chem. Res. 49 (2016) 2355.
[15] V. Viswam, J. Dragas, A. Shadmani, Y. Chen, A. Stettler, J. Müller, A. Hierlemann, Multi-functional microelectrode array system featuring 59,760 electrodes, 2048 electrophysiology channels, impedance and neurotransmitter measurement units, in: 2016 IEEE International Solid-State Circuits Conference, ISSCC, 2016, pp. 394–396.
[16] Y. Jiang, X. Liu, T.C. Dang, M. Yan, H. Yu, J.C. Huang, C.H. Hsieh, T.T. Chen, A 512 × 576 65-nm CMOS ISFET sensor for food safety screening with 123.8 mV/pH sensitivity and 0.01 pH resolution, in: 2016 IEEE Symposium on VLSI Technology, 2016, pp. 1–2.
[17] M. Ballini, J. Müller, P. Livi, Y. Chen, U. Frey, A. Stettler, A. Shadmani, V. Viswam, I.L. Jones, D. Jäckel, M. Radivojevic, M.K. Lewandowska, W. Gong, M. Fiscella, D.J. Bakkum, F. Heer, A. Hierlemann, A 1024-channel CMOS microelectrode array with 26,400 electrodes for recording and stimulation of electrogenic cells in vitro, IEEE J. Solid-State Circuits 49 (2014) 2705–2719.
[18] C.M. Lopez, H.S. Chun, L. Berti, S. Wang, J. Putzeys, C.V.D. Bulcke, J.W. Weijers, A. Firrincieli, V. Reumers, D. Braeken, N.V. Helleputte, A 16384-electrode 1024-channel multimodal CMOS MEA for high-throughput intracellular action potential measurements and impedance spectroscopy in drug-screening applications, in: 2018 IEEE International Solid - State Circuits Conference, ISSCC, 2018, pp. 464–466.
[19] J.S. Park, M.K. Aziz, S. Li, T. Chi, S.I. Grijalva, J.H. Sung, H.C. Cho, H. Wang, 1024-pixel CMOS multimodality joint cellular sensor/stimulator array for real-time holistic cellular characterization and cell-based drug screening, IEEE Trans. Biomed. Circuits Syst. 12 (2018) 80–94.
[20] J.R. Stetter, E.F. Stetter, M.T. Carter, Abundant Chemical Sensors and the Trillion Sensor Universe, Meeting Abstracts, vol. 6, The Electrochemical Society, 2014, p. 451.
[21] W.P. Gouveia, J.A. Scales, Bayesian seismic waveform inversion: parameter estimation and uncertainty analysis, J. Geophys. Res., Solid Earth 103 (1998) 2759–2779.

[22] T. Iizumi, M. Yokozawa, M. Nishimori, Parameter estimation and uncertainty analysis of a large-scale crop model for paddy rice: application of a Bayesian approach, Agric. For. Meteorol. 149 (2009) 333–348.
[23] F. Feng, T.B. Kepler, Bayesian estimation of the active concentration and affinity constants using surface plasmon resonance technology, PLoS ONE 10 (2015) e0130812.
[24] N. Petra, C.G. Petra, Z. Zhang, E.M. Constantinescu, M. Anitescu, A Bayesian approach for parameter estimation with uncertainty for dynamic power systems, IEEE Trans. Power Syst. 32 (2017) 2735–2743.
[25] J. Chen, B. McGaughy, D. Sylvester, C. Hu, An on-chip, attofarad interconnect charge-based capacitance measurement (CBCM) technique, in: Proc. IEDM, 1996, pp. 69–72.
[26] A. Cossettini, M. Dalla Longa, P. Scarbolo, L. Selmi, Modeling and simulation of small CCMV virus detection by means of high frequency impedance spectroscopy at nanoelectrodes, in: 2017 IEEE 17th International Conference on Nanotechnology, IEEE-NANO, 2017, pp. 416–419.
[27] A. Cossettini, L. Selmi, On the response of nanoelectrode impedance spectroscopy measures to plant, animal, and human viruses, IEEE Trans. Nanobiosci. 17 (2018) 102–109.
[28] A.J. Bard, L.R. Faulkner, Electrochemical Methods: Fundamentals and Applications, second ed., John Wiley & Sons, 2001.
[29] H.V. Helmholtz, Studien über electrische Grenzschichten, Ann. Phys. 243 (1879) 337–382.
[30] M. Gouy, Sur la constitution de la charge électrique à la surface d'un électrolyte, J. Phys. Theor. Appl. 9 (1910) 457–468.
[31] D.L. Chapman LI, A contribution to the theory of electrocapillarity, Philos. Mag. 25 (1913) 475–481.
[32] O. Stern, Zur Theorie der elektrolytischen Doppelschicht, Ber. Bunsenges. Phys. Chem. 30 (1924) 508–516.
[33] J. Rosenstein, V. Ray, M. Drndic, K.L. Shepard, Nanopore DNA sensors in CMOS with on-chip low-noise preamplifiers, in: 2011 16th International Solid-State Sensors, Actuators and Microsystems Conference, TRANSDUCERS, 2011, pp. 874–877.
[34] C. Stagni, C. Guiducci, L. Benini, B. Ricco, S. Carrara, C. Paulus, M. Schienle, R. Thewes, A fully electronic label-free DNA sensor chip, IEEE Sens. J. 7 (2007) 577–585.
[35] P. Scarbolo, E. Accastelli, F. Pittino, T. Ernst, C. Guiducci, L. Selmi, Characterization and modelling of differential sensitivity of nanoribbon-based pH-sensors, in: 2015 Transducers – 2015 18th International Conference on Solid-State Sensors, Actuators and Microsystems, TRANSDUCERS, 2015, pp. 2188–2191.
[36] S. Rigante, P. Scarbolo, M. Wipf, R.L. Stoop, K. Bedner, E. Buitrago, A. Bazigos, D. Bouvet, M. Calame, C. Schönenberger, et al., Sensing with advanced computing technology: fin field-effect transistors with high-k gate stack on bulk silicon, ACS Nano 9 (2015) 4872–4881.
[37] L. Bousse, P. Bergveld, On the impedance of the silicon dioxide/electrolyte interface, J. Electroanal. Chem. Interfacial Electrochem. 152 (1983) 25–39.
[38] C. Menzel, T. Lerch, T. Scheper, K. Schügerl, Development of biosensors based on an electrolyte isolator semiconductor (EIS)-capacitor structure and their application for process monitoring. Part I. Development of the biosensors and their characterization, Anal. Chim. Acta 317 (1995) 259–264.
[39] M.H. Abouzar, W. Moritz, M.J. Schöning, A. Poghossian, Capacitance–voltage and impedance-spectroscopy characteristics of nanoplate EISOI capacitors, Phys. Status Solidi A 208 (2011) 1327–1332.
[40] N. Couniot, A. Afzalian, N. Van Overstraeten-Schlögel, L. Francis, D. Flandre, Capacitive biosensing of bacterial cells: analytical model and numerical simulations, Sens. Actuators B, Chem. 211 (2015) 428–438.
[41] P.R. Nair, M.A. Alam, Screening-limited response of nanobiosensors, Nano Lett. 8 (2008) 1281–1285.
[42] Y. Liu, R.W. Dutton, Effects of charge screening and surface properties on signal transduction in field effect nanowire biosensors, J. Appl. Phys. 106 (2009) 014701.
[43] Y. Wang, G. Li, Performance investigation for a silicon nanowire FET biosensor using numerical simulation, in: Proc. IEEE Nanotechnology Materials and Devices Conference, 2010, pp. 81–86.
[44] S. Baumgartner, M. Vasicek, A. Bulyha, C. Heitzinger, Optimization of nanowire DNA sensor sensitivity using self-consistent simulation, Nanotechnology 22 (2011) 425503.
[45] S. Baumgartner, C. Heitzinger, Existence and local uniqueness for 3d self-consistent multiscale models of field-effect sensors, Commun. Math. Sci. 10 (2012) 693–716.
[46] A. Flavell, M. Machen, B. Eisenberg, J. Kabre, C. Liu, X. Li, A conservative finite difference scheme for Poisson-Nernst-Planck equations, J. Comput. Electron. (2013) 1–15.
[47] F. Pittino, L. Selmi, Use and comparative assessment of the CVFEM method for Poisson-Boltzmann and Poisson-Nernst-Planck three dimensional simulations of impedimetric nano-biosensors operated in the DC and AC small signal regimes, Comput. Methods Appl. Mech. Eng. (2014) 902–923.
[48] F. Pittino, L. Selmi, A technique to model the AC response of diffuse layers at electrode/electrolyte interfaces and to efficiently simulate impedimetric biosensor arrays for many analyte configurations, in: Proceedings of the International Conference on Simulation of Semiconductor Processes and Devices, SISPAD, 2014, pp. 353–356.
[49] C. Heitzinger, L. Taghizadeh, Analysis of the drift-diffusion-Poisson-Boltzmann system for nanowire and nanopore sensors in the alternating-current regime, Commun. Math. Sci. 15 (2017) 2303–2325.
[50] L. Taghizadeh, A. Khodadadian, C. Heitzinger, The optimal multilevel Monte-Carlo approximation of the stochastic drift-diffusion-Poisson system, Comput. Methods Appl. Mech. Eng. 318 (2017) 739–761.
[51] P. Scarbolo, F. Pittino, M. Dalla Longa, A. Cossettini, L. Selmi, ENBIOS-1D Lab, https://nanohub.org/resources/23272, 2017, https://doi.org/10.4231/D3GX44W13 [Online]. Available: https://nanohub.org/resources/biolab.
[52] A. Hoxha, P. Scarbolo, A. Cossettini, F. Pittino, L. Selmi, ENBIOS-2D Lab, https://nanohub.org/resources/24698, https://doi.org/10.4231/D3V11VM7D, [Online]. Available: https://nanohub.org/resources/biolabisfet.
[53] J. Schöberl, NETGEN an advancing front 2D/3D-mesh generator based on abstract rules, Comput. Vis. Sci. 1 (1997) 41–52.
[54] F. Pittino, Prospects of Nanoelectronic Biosensing With High-Frequency Impedance Spectroscopy, Ph.D. thesis, DIEGM, University of Udine, Udine, Italy, 2015.
[55] R. van Hal, J. Eijkel, P. Bergveld, A general model to describe the electrostatic potential at electrolyte oxide interfaces, Adv. Colloid Interface Sci. 69 (1996) 31–62.
[56] A. Cossettini, L. Selmi, Calibration of high-frequency impedance spectroscopy measurements with nanocapacitor arrays, in: Proc. 2nd European Biosensor Symposium, EBS2019, Florence, Italy, 2019, p. 131.
[57] A. Cossettini, Investigation and Development of CMOS Pixelated Nanocapacitor Biosensors for Quantitative Analyses, Ph.D. thesis, DPIA - University of Udine, Udine, Italy, 2019.
[58] L. Taghizadeh, B. Stadlbauer, C. Heitzinger, Bayesian inversion for electrical-impedance tomography, 2018, Submitted for publication.
[59] S.L. Cotter, G.O. Roberts, A.M. Stuart, D. White, MCMC methods for functions: modifying old algorithms to make them faster, Stat. Sci. (2013) 424–446.
[60] R. Neal, MCMC using ensambles of states for problems with fast and slow variables such as Gaussian process regression, arXiv:1101.0387, 2011.
[61] L. Martino, A review of multiple try MCMC algorithms for signal processing, Digit. Signal Process. 75 (2018).
[62] R. Neal, M. Radford, MCMC using Hamiltonian dynamics, in: S. Brooks, A. Gelman, G.L. Jones, X.-L. Meng (Eds.), Handbook of Markov Chain Monte Carlo, Chapman and Hall/CRC, 2011.
[63] K.M. Hanson, Markov Chain Monte Carlo Posterior Sampling With the Hamiltonian Method, Medical Imaging 2001: Image Processing, vol. 4322, International Society for Optics and Photonics, 2001, pp. 456–467.

[64] M. Girolami, B. Calderhead, Riemann manifold Langevin and Hamiltonian Monte Carlo methods, J. R. Stat. Soc., Ser. B, Stat. Methodol. 73 (2011) 123–214.
[65] S. Brooks, G. Roberts, Convergence assessment techniques for Markov chain Monte Carlo, Stat. Comput. 8 (1998) 319–335.
[66] A. Gelman, J. Carlin, H. Stern, D. Dunson, A. Vehtari, D. Rubin, Bayesian Data Analysis, 3rd ed., Taylor & Francis Group, Boca Raton, FL, 2013.
[67] J. Bezanson, et al., Julia: the Julia programming language, v1.0, https://julialang.org/, 2018.